CORA Cork Open Research Archive
Cartlann Taighde Oscailte Chorcaí

Title	Nonstationary coupling between heart rate and perfusion index in extremely preterm infants in the first day of life
Authors	O'Toole, John M.;Dempsey, Eugene M.;Van Laere, David
Publication date	2021-02-05
Original Citation	O'Toole, J. M., Dempsey, E. M. and Van Laere, D. (2021) 'Nonstationary coupling between heart rate and perfusion index in extremely preterm infants in the first day of life', Physiological Measurement, 42(3), 035005 (16pp). https://doi.org/10.1088/1361-6579/abe3de
Type of publication	Article (peer-reviewed)
Link to publisher's version	10.1088/1361-6579/abe3de
Rights	© 2021, Institute of Physics and Engineering in Medicine. As the Version of Record of this article is going to be/has been published on a subscription basis, this Accepted Manuscript will be available for reuse under a CC BY-NC-ND 3.0 licence after a 12 month embargo period. - https://creativecommons.org/licenses/by-nc-nd/3.0/
Download date	2026-10-30 00:47:45
Item downloaded from	https://hdl.handle.net/10468/11080



University College Cork, Ireland
Coláiste na hOllscoile Corcaigh

Physiological Measurement

IPEM Institute of Physics and Engineering in Medicine

ACCEPTED MANUSCRIPT

Nonstationary coupling between heart rate and perfusion index in extremely preterm infants in the first day of life

To cite this article before publication: John M O'Toole *et al* 2021 *Physiol. Meas.* in press https://doi.org/10.1088/1361-6579/abe3de

Manuscript version: Accepted Manuscript

Accepted Manuscript is "the version of the article accepted for publication including all changes made as a result of the peer review process, and which may also include the addition to the article by IOP Publishing of a header, an article ID, a cover sheet and/or an 'Accepted Manuscript' watermark, but excluding any other editing, typesetting or other changes made by IOP Publishing and/or its licensors"

This Accepted Manuscript is **© 2021 Institute of Physics and Engineering in Medicine**.

During the embargo period (the 12 month period from the publication of the Version of Record of this article), the Accepted Manuscript is fully protected by copyright and cannot be reused or reposted elsewhere.
As the Version of Record of this article is going to be / has been published on a subscription basis, this Accepted Manuscript is available for reuse under a CC BY-NC-ND 3.0 licence after the 12 month embargo period.

After the embargo period, everyone is permitted to use copy and redistribute this article for non-commercial purposes only, provided that they adhere to all the terms of the licence https://creativecommons.org/licences/by-nc-nd/3.0

Although reasonable endeavours have been taken to obtain all necessary permissions from third parties to include their copyrighted content within this article, their full citation and copyright line may not be present in this Accepted Manuscript version. Before using any content from this article, please refer to the Version of Record on IOPscience once published for full citation and copyright details, as permissions will likely be required. All third party content is fully copyright protected, unless specifically stated otherwise in the figure caption in the Version of Record.

View the article online for updates and enhancements.

This content was downloaded from IP address 143.239.102.69 on 12/02/2021 at 10:43

Nonstationary coupling between heart rate and perfusion index in extremely preterm infants in the first day of life

J M O'Toole[1,2], E M Dempsey[1,2] and D Van Laere[3,4]

[1] INFANT Research Centre, University College Cork, Cork, Ireland.
[2] Department of Paediatrics and Child Health, University College Cork, Cork, Ireland.
[3] Department of Neonatal Intensive Care, University Hospital Antwerp, Edegem, Belguim.
[4] Laboratory of Pediatrics, Department of Life Sciences, University of Antwerp, Belgium.

E-mail: jotoole@ucc.ie, g.dempsey@ucc.ie, david.vanlaere@uza.be

Abstract. *Objective:* Adaptation to the extra-uterine environment presents many challenges for infants born less than 28 weeks of gestation. Quantitative analysis of readily-available physiological signals at the cotside could provide valuable information during this critical time. We aim to assess the time-varying coupling between heart rate (HR) and perfusion index (PI) over the first 24 hours after birth and relate this coupling to gestational age, inotropic therapy, and short-term clinical outcome. *Approach:* We develop new nonstationary measures of coupling to summarise both frequency- and direction-dependent coupling. These measures employ a coherence measure capable of measuring time-varying Granger casuality using a short-time information partial directed coherence function. Measures are correlated with gestational age, inotropic therapy (yes/no), and outcome (adverse/normal). *Main Results:* In a cohort of 99 extremely preterm infants (<28 weeks of gestation), we find weak but significant coupling in both the HR→PI and PI→HR directions ($P < 0.05$). HR→PI coupling increases with maturation (correlation $r = 0.26$; $P = 0.011$); PI→HR coupling increases with inotrope administration ($r = 0.27$; $P = 0.007$). And nonstationary features of PI→HR coupling are associated with adverse outcome ($r = 0.27$; $P = 0.009$). *Significance:* Nonstationary features are necessary to distinguish different coupling types for complex biomedical systems. Time-varying directional coupling between PI and HR provides objective and independent biomarkers of adverse outcome in extremely preterm infants.

Keywords: neonate, preterm infant, heart rate, perfusion index, coupling, Granger casuality, non-stationary connectivity, instantaneous frequency, cardiovascular instability

Submitted to: *Physiological Measurement*

Accepted Manuscript

1. Introduction

Premature birth forces an immature cardiovascular system to adapt to the extra-uterine environment. For the extremely preterm infant, born less than 28 weeks of gestation, this postnatal transition often causes haemodynamic instability and inadequate cerebral perfusion (Gill, 2019). The immature myocardium may not be capable of the required cardiac output to maintain stable end-organ perfusion. In addition, systemic vascular resistance may fail to ensure adequate blood flow also leading to inadequate end-organ perfusion. As a consequence, up to 1 in 3 infants in this age group are likely to develop a brain injury over the first few days after birth (Stoll *et al.*, 2010). These injuries can lead to death or impaired neurodevelopment with potentially life-long disabilities (Bolisetty *et al.*, 2014).

Cranial ultrasounds are used diagnose brain injury in preterm infants. This monitoring, however, can only present a snapshot in time and therefore may miss an evolving injury. Computer-based analysis of continuous physiological signals has the potential to provide real-time detection of injuries at the cotside. An important first step to a fully automated system is a thorough quantitative analysis of suitable physiological signals (Van Laere *et al.*, 2018).

Previous work has demonstrated a relation between specific physiological signals and short-term clinical outcome, including brain injury. For example, distinct quantitative characteristics of the electroencephalogram (EEG) (Iyer *et al.*, 2015), cerebral oxygenation (O'Toole *et al.*, 2016; Kenosi *et al.*, 2017; O'Toole *et al.*, 2018; Katheria *et al.*, 2018), and perfusion index (Van Laere *et al.*, 2016) demonstrate an association with adverse outcome. The interaction, or coupling, between different physiological signals can provide further information on the complex haemodynamic system. A recent study examined the interaction between cerebral oxygenation and heart rate (HR), peripheral oxygen saturation, and perfusion index (PI) (Beausoleil *et al.*, 2018), finding that coupling between the signals are related to brain injury and pulmonary haemorrhage. Another recent study examined the interaction between multiple physiological signals, including cerebral activity (EEG), cerebral oxygenation, and systemic signals (HR, peripheral oxygen saturation, and blood pressure) (Hendrikx *et al.*, 2018). This study found propofol administration decreased coupling between signals. These studies, however, use monitoring technologies, such as near infrared spectroscopy and EEG, that are typically not readily available in most neonatal intensive care units.

We aim to examine the interaction between two readily-available physiological signals, HR and PI, over the first day of life for a cohort of extremely preterm infants. HR is a common physiological signal monitored in neonatal intensive care. PI is not routinely displayed on a cotside monitor but can be easily recorded from the pulse oximeter (Van Laere *et al.*, 2016; Alderliesten *et al.*, 2015; Hawkes *et al.*, 2015; Kinoshita *et al.*, 2013; Cresi *et al.*, 2010). The signal measures the ratio of pulsatile to non-pulsatile components and represents a quantifiable measure of peripheral perfusion. As HR is

Accepted Manuscript

an important component in cardiac output and PI a measure of end-organ perfusion, HR–PI interaction is likely to be mediated by the cardiovascular system. An immature cardiovascular system can lead to haemodynamic instability, which, in turn, can lead to insufficient end-organ perfusion. We investigate HR–PI interaction as a means of capturing this haemodynamic instability.

We relate this coupling to clinical relevant information, namely gestational age (GA), inotropic therapy for treating hypotension, and short-term clinical outcome. Short-term outcome is defined as early mortality before 72 hours of life, acquired severe intra-ventricular haemorrhage (IVH), or severe cystic periventricular leukomalacia (O'Toole *et al.*, 2016; Van Laere *et al.*, 2016; O'Toole *et al.*, 2018). We make no assumptions about the nature of the coupling between the signals and therefore employ non-stationary methods which determine the direction of influence using Granger causality. In addition, we also develop new features to summarise the coupling without compromising the nonstationarity and directionality of the methods. These methods are freely available as Matlab code (https://github.com/otoolej/nonstat_directional_coupling).

2. Materials and Methods

Before estimating the Granger causality methods, we first extract a slowly varying baseline from both the HR and PI signals. Removing this trend component from the signal allows us to focus on the oscillations of the signals around a slowly-varying mean value but not the mean value itself. We refer to this higher-frequency component as the detrend component (Van Laere *et al.*, 2016). We also determine coupling on a longer time scale by using the trend components.

2.1. Patients, data acquisition, and pre-processing

HR and PI were collected from extremely preterm infants (<28 weeks GA) at the neonatal intensive care unit of the University Hospital of Antwerp, Edegem, Belgium, between January 1, 2012, and December 31, 2014. Infants were excluded from the study if they were transferred into the unit after a postnatal age of 24 hours, had congenital heart disease, or were considered nonviable. The study was approved by the Committee for Medical Ethics of the University Hospital Antwerp (reference 15/32/326) with a waiver of informed consent. This is the same cohort of 99 infants from a previous Van Laere *et al.* (2016) study. Median GA is 26.7 weeks, with an inter-quartile range (IQR) of 24.1 to 24.2 weeks (range: 24.1 to 27.9 weeks). Median duration for the PI signal is 24.0 hours (IQR: 23.0 to 24.0 hours; range: 13.8 to 24.0 hours) and median duration of the HR signal is 23.9 hours (IQR: 23.6 to 24.0 hours; range: 13.8 to 24.0 hours).

All infants had a cranial ultrasound as soon as possible after birth with follow-up scans daily over the first 3 days of life and weekly thereafter. Infants with a severe IVH on the initial scan after birth were excluded from further analysis. Severe IVH

Accepted Manuscript

was defined as grade 3 or 4 injury. These infants were excluded to focus on acquired neonatal injury. Short-term clinical outcome was dichotomised as normal and adverse. Adverse outcome was determined by patients who died within 72 hours after birth, or were diagnosed with an acquired severe IVH or severe periventricular leukomalacia on serial scans; otherwise infants were grouped as normal (O'Toole *et al.*, 2016; Van Laere *et al.*, 2016; O'Toole *et al.*, 2018).

Basic pre-processing steps are applied to both signals. To remove artefacts in the HR signal, we remove values of HR with a derivative greater than 60 bpm; that is, if $|h[n] - h[n-1]| > 60$, for HR signal $h[n]$, then remove $h[n]$ at sample n. Likewise, for the PI signal $p[n]$, if $|p[n] - p[n-1]| > 2$, then remove $p[n]$ at sample n and all points within a 2-minute collar around n. These sharp spikes in PI are associated with probe movement. Next the HR and PI signals are split into trend and detrend components by applying a low-pass filter to calculate the trend. The low-pass filter has a cut-off of 1/43.2 mHz, a frequency with a period of approximately 12 hours, and is implemented using a finite-impulse response filter with a Blackman–Harris window of 501 samples. Filtering is computed in a forward and backward process to ensure zero-phase. The detrend component is equal to the signal minus the trend component.

2.2. Coupling between HR and PI trends

To assess for coupling on a long-duration time scale, we correlate the HR and PI trend components. We use Spearman's correlation coefficient to assess for coupling between the trends. Spearman's correlation is calculated by first converting the signals, the length-N $x_l[n]$ and $x_q[n]$, to ranks, denoted as $r_l[n]$ and $r_q[n]$. The covariance of $r_l[n]$ and $r_q[n]$ is divided by the product of the individual standard deviations σ_l and σ_q,

$$\begin{aligned} t_1 &= \frac{\operatorname{cov}(r_l[n], r_q[n])}{\sigma_l \sigma_q} \\ &= \frac{\frac{1}{N-1}\sum_{n=0}^{N-1}(r_l[n] - \overline{r}_l[n])(r_q[n] - \overline{r}_q[n])}{\sqrt{\frac{1}{N-1}\sum_{n=0}^{N-1}(r_l[n] - \overline{r}_l[n])^2 \frac{1}{N-1}\sum_{n=0}^{N-1}(r_q[n] - \overline{r}_q[n])^2}} \end{aligned} \tag{1}$$

where $\overline{r}[n] = 1/N \sum_{n=0}^{N-1} r[n]$ is the mean of signal $r[n]$.

For each infant, we generate a correlation coefficient and test whether this correlation is significant or not. We do so by generating a 95% confidence interval (CI) using a bootstrap procedure with 1 000 iterations. If the CIs include 0, the correlation coefficient is considered non-significant and set to 0. As the correlation summaries the temporal information over the 24-hour period, this coupling measure is stationary in nature.

2.3. Time-varying Granger causality

To estimate Granger causality between the HR and PI detrend components we use the information partial directed coherence (iPDC) function (Takahashi *et al.*, 2010). The

Accepted Manuscript

iPDC is an improved version of partial-directed coherence, as it is invariant to signal amplitudes, relates to information flow, and represents a frequency-dependent effect-size measure for the magnitude of connection (Takahashi *et al.*, 2010).

The iPDC is defined for a multivariate signal as follows. A stationary, zero-mean, multivariate process $\mathbf{x}[n] = (x_1[n]\ x_2[n] \dots\ x_K[n])^{\mathsf{T}}$, can be represented as a multivariate auto-regressive model (MVAR)

$$\mathbf{x}[n] = \sum_{m=1}^{p} \mathbf{A}[m]\mathbf{x}[n-m] + \mathbf{w}[n] \tag{2}$$

for model order-p with $\mathbf{w}[n] = (w_1[n]\ w_2[n] \dots w_K[n])^{\mathsf{T}}$ as the innovation processes (superscript T represents the transpose operation). This stationary Gaussian process has covariance matrix $\mathbf{\Sigma_w}$ with elements σ^2_{kq}. The MVAR coefficient matrices are described as a sequence of matrices

$$\mathbf{A}[m] = \begin{pmatrix} a^m_{1,1} & a^m_{1,2} & \cdots & a^m_{1,K} \\ a^m_{2,1} & a^m_{2,2} & \cdots & a^m_{2,K} \\ \vdots & \vdots & \ddots & \vdots \\ a^m_{K,1} & a^m_{K,2} & \cdots & a^m_{K,K} \end{pmatrix}$$

for $m = 1, 2, \dots, p$. These coefficients are transformed to the frequency domain as follows:

$$\mathbf{B}_{lq}[k] = \begin{cases} 1 - \sum_{m=1}^{p} a^m_{lq} \mathrm{e}^{-\mathrm{j}2\pi km} & \text{if } k = q \\ -\sum_{m=1}^{p} a^m_{lq} \mathrm{e}^{-\mathrm{j}2\pi km} & \text{otherwise} \end{cases} \tag{3}$$

and used to define the iPDC from signal $x_l[n]$ to $x_q[n]$ as

$$\pi_{lq}[k] = \frac{\mathbf{B}_{lq}[k]}{\sqrt{\sigma^2_{ll}\mathbf{b}^{\mathsf{H}}_q[k]\mathbf{\Sigma}^{-1}_{\mathbf{w}}\mathbf{b}_q[k]}} \tag{4}$$

where $\mathbf{b}^{\mathsf{H}}$ denotes the Hermitian transpose of $\mathbf{b}$ and where

$$\mathbf{b}_q[k] = (\mathbf{B}_{1q}[k]\ \mathbf{B}_{2q}[k] \dots \mathbf{B}_{Kq}[k])^{\mathsf{T}}$$

As p is a small number, typically < 10, $\mathbf{A}[m]$ is zero-padded from length-p to length-M with $M > p$, to increasing the sampling frequency in the frequency-domain iPDC $\pi_{lq}[k]$. The magnitude of iPDC, $|\pi_{lq}[k]|^2$, represents the frequency-dependent coupling between signals $x_l[n]$ and $x_q[n]$.

Although $|\pi_{lq}[k]|^2$ presents a normalised effect size of the connectivity at each discrete frequency k, it lacks information on the statistical validity of effect size. To address this shortfall, Baccala *et al.* (2013) developed a closed-form expression for the (asymptotic) statistical behaviour of the iPDC and with it a means for testing the null hypothesis that $\pi_{lq}[k] = 0$. With this expression we can develop a threshold at a pre-described level of significance, for example with $\alpha = 0.05$, below which we assume that the iPDC represents the zero level. This threshold is frequency-dependent and differs

Accepted Manuscript

depending on coupling between l and q. Full details can be found in Baccala *et al.* (2013).

To incorporate non-stationary causality, we simply generate a short-time version by first windowing the signals and then generating the iPDC for each windowed segment:

$$S_{lq}[n,k] = \pi\left(w[m]x_l[m-nR], w[m]x_q[m-nR]; k\right) \tag{5}$$

for $0 \leq m \leq L-1$, using the notation $\pi(x, y; k)$ to represent iPDC in (4) between signals x and y. The short-time segments $w[m]x_l[m-nR]$ are generated with length-L window $w[n]$ and hop size R. The magnitude of the short-time iPDC (ST-iPDC) function, $|S_{lq}[n,k]|^2$, is a two-dimensional time–frequency representation, similar in concept to the spectrogram.

To compare the ST-iPDC with the standard coherence function we generate a short-time coherence $C_{lq}[n,k]$ function using the same approach in (5), as

$$C_{lq}[n,k] = \rho\left(w[m]x_l[m-nR], w[m]x_q[m-nR]; k\right) \tag{6}$$

for $0 \leq m \leq L-1$. Coherence function $\rho[k]$ is estimated as

$$\rho_{lq}[k] = \frac{|U_{lq}[k]|^2}{P_{ll}[k]P_{qq}[k]} \tag{7}$$

where $U_{lq}[k]$ is cross spectral density estimate between $x_l[n]$ and $x_q[n]$ and $P_{ll}[l]$ is the auto spectral density. To estimate the level of zero coherence in $\rho[k]$, the Fourier-transform shuffling method generates surrogate, uncoupled signals to estimate the null-hypothesis distribution (that is, $\rho[k] = 0$). The method is described in more detail in O'Toole and Boylan (2017).

2.4. Implementation of ST-iPDC

The following describes the implementation used to compute ST-iPDC and associated features for the HR and PI detrend components. First, we segment the components into 3-hour epochs using a rectangle window $w[n]$ with a hop size [R in (5)] of 5%. Second, we remove the linear trend from all epochs to ensure there is no mean offset before estimating the MVAR. Third, we estimate the MVAR coefficients $\mathbf{A}[m]$ and covariance matrix $\mathbf{\Sigma}_w$ in (2). Model order for the MVAR, p in (2), is estimated using the log of Akaike's final prediction error (Neumaier and Schneider, 2001), searching up to a maximum order of 10. To test if the MVAR is an appropriate fit to the HR and PI epochs, we test the assumption that the residuals, $\mathbf{w}[n]$ in (2), are uncorrelated using the Li–McLeod Portmanteau statistic (Schneider and Neumaier, 2001). If we find significant correlations ($P < 0.05$), then the current epoch is excluded from the analysis.

Fourth, we estimate the iPDC in (4) removing coherence values at k if below the threshold. This statistical threshold is estimated from the asymptotic statistics of the iPDC (Baccala *et al.*, 2013). Although $N = 180$ is small in our case, these methods are robust to violations of the asymptotic assumptions (Baccala *et al.*, 2013). Fifth, we iterate this process for all epochs to generate the ST-iPDC in (5) at time points n.

Accepted Manuscript

For the coherence function in (7) we use Welch spectral estimates with a Hamming window of length 71 samples with 75% overlap. The null distribution is generated using 500 iterations of the random-phase surrogate signals with the cut-off for non-zero coherence set to $P < 0.01$ (O'Toole and Boylan, 2017).

2.5. Nonstationary features of the ST-iPDC

To make use of the time-varying frequency content of the coupling, we first estimate the predominate frequency coupling at each time instance and then characterise this temporal trajectory by summarising with a number of quantitative features. First, the nonstationary (time-varying) frequency is computed by estimating the median frequency at each time step by selecting $f_{lq}[n]$ that satisfies the following relation:

$$\sum_{k=0}^{f_{lq}[n]} |S_{lq}[n,k]|^2 = \frac{1}{2}\sum_{k=0}^{M} |S_{lq}[n,k]|^2 \tag{8}$$

As this relation may not be exact we interpolate the cumulative distribution on the left-hand side with piece-wise cubic interpolation when estimating $f_{lq}[n]$. Thus the 2D $|S_{lq}[n,k]|^2$ is compressed into the 1D instantaneous frequency (IF) $f_{lq}[n]$. Second, to extract characteristics of this temporal trajectory, we estimate features on $f_{lq}[n]$, namely the standard deviation of $f_{lq}[n]$ and the Hjorth parameters. As $f_{lq}[n]$ is not zero-mean, we use the original definition for the 3 Hjorth parameters (Hjorth, 1970), defining activity, mobility, and complexity as follows:

$$d_1 = \frac{1}{N}\sum_{n=0}^{N-1} f^2[n], \qquad d_2 = \sqrt{\frac{\frac{1}{N}\sum_{n=0}^{N-1}\dot{f}^2[n]}{d_1}}, \qquad d_3 = \frac{1}{d_2}\left(\sqrt{\frac{\sum_{n=0}^{N-1}\ddot{f}^2[n]}{\sum_{n=0}^{N-1}\dot{f}^2[n]}}\right) \tag{9}$$

where $\dot{f}[n]$ represents the derivative of $f[n]$ and $\ddot{f}[n]$ represents the derivative of $\dot{f}[n]$, assuming that $f[n]$ is length N. We drop the sub-script l, q notation here for simplicity. We use an finite-impulse response filter of length-$N/4$ to compute the derivatives $\dot{f}[n]$ and $\ddot{f}[n]$. The linear-phase filter is defined using a least-squares method to approach the ideal response $|H[k]| = k$ for frequencies from 0 to $0.45f_s$, where f_s is the sampling frequency, and tailing to zero for $0.45f_s$ to $0.5f_s$. The standard deviation of $f[n]$ is defined as

$$d_4 = \sqrt{\frac{1}{N-1}\sum_{n=0}^{N-1}\left(f[n] - \overline{f}[n]\right)^2} \tag{10}$$

where $\overline{f}[n]$ represents the mean-value of $f[n]$. Thus $\{d_1, d_2, d_3, d_4\}$ represents our nonstationary feature set, estimated on each $f_{lq}[n]$ instantaneous frequency extracted from ST-iPDC $|S_{lq}[n,k]|^2$. And lastly, to include a summative measure of coupling, we sum over time and frequency for the 2D ($N \times M$) ST-iPDC

$$d_5 = \frac{1}{NM}\sum_{k=0}^{M-1}\sum_{n=0}^{N-1} |S_{lq}[n,k]|^2 \tag{11}$$

Accepted Manuscript

Although this feature set captures the nonstationary characteristics of the 2 ST-iPDCs, it does not capture how the relative coupling between HR → PI and PI → HR changes over time. To address this, we propose the following. First we, estimate the time-marginal of the ST-iPDC, as

$$\phi_{lq}[n] = \frac{1}{M}\sum_{k=0}^{M} |S_{lq}[n,k]|^2 \tag{12}$$

and then generate a plot of the trajectory $(\phi_{12}[n], \phi_{21}[n])$ for $n = 0, 1, \ldots, N-1$. From this plot, bounded within $[0, 1]$, we estimate three features: the fractal dimension, magnitude of the centroid, and angle of the centroid. To estimate the fractal dimension, we extend the method proposed by Higuchi (1990) from a time-series to a 2D plane curve. The Higuchi method computes curve length, using the Euclidean distance between points, at different scales $k = 1, 2, \ldots, k_{\max}$. Thus, for curve $(x[n], y[n])$, we estimate the average length between points as

$$L_m(k) = \frac{1}{k^2\lfloor\frac{N-m}{k}\rfloor}\sum_{i=1}^{\lfloor\frac{N-m}{k}\rfloor} \sqrt{\{x[m+ik]-x[m+(i-1)k]\}^2 + \{y[m+ik]-y[m+(i-1)k]\}^2} \tag{13}$$

at different starting points $m = 1, 2, \ldots, k$, including the scaling factor $1/k^2$ (Higuchi, 1990). Typically, $L_m(k)$ is averaged (mean) over all m to generate $L(k)$ and a line is fitted to points $(\log\{1/k\}, \log\{L(k)\})$. The slope of this line produces the fractal dimension, D. We make 2 changes here to increase statistical robustness. First, we take the median of $L_m(k)$ over m instead of the mean value. Second, we estimate D as the median of scale-dependent fractal dimension $\hat{D}[k]$. This function $\hat{D}[k]$ captures the sensitivity of D to different scale values and is calculated as the derivative of $-\log\{L(k)\}$ over the derivative of $\log\{k\}$ (Higuchi, 1990), which simplifies to

$$\hat{D}[k] = -\frac{\log\{L(k)/L(k-1)\}}{\log\{k/(k-1)\}}, \qquad \text{for } k = 2, 3, \ldots, k_{\max}$$

using the first-order difference method. An example of the method for three curves with increasing levels of disorder are presented in Figure 1. For our application, we replace $(x[n], y[n])$ in (13) with $(\phi_{12}[n], \phi_{21}[n])$ and denote the fractal dimension measure as d_6. In initial testing with the physiological data, we found that d_6 tends to overestimate the fractal dimension. To ensure that the estimates are bounded within $[1, 2]$, we follow a procedure proposed by Higuchi (1990) that integrates the signal before calculating the fractal dimension. For our plane curve, we integrate over one dimension by substituting $\phi_{12}^{\Sigma}[n] = \sum_{i=1}^{n}\phi_{12}[i]$ for $\phi_{12}[n]$ before calculating (13).

Next, we estimate the centroid of the Cartesian coordinates as

$$\mathbf{c} = \left(\frac{1}{N}\sum_{n=0}^{N-1}\phi_{12}[n], \frac{1}{N}\sum_{n=0}^{N-1}\phi_{21}[n]\right).$$

and then transform to polar coordinates to calculate the magnitude, $d_7 = \sqrt{c_1^2 + c_2^2}$, and angle $d_8 = \cos^{-1}(c_2/d_7)$.

Accepted Manuscript

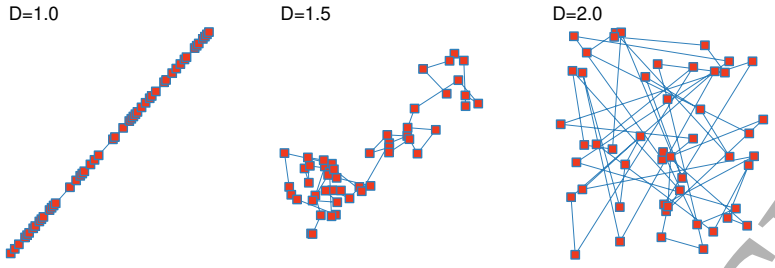


Figure 1. Fractal dimension (FD) estimate for 3 different plane curves. Left: linear curve $(l[n], l[n])$ with non-uniform sampling. Middle: coloured Gaussian noise $(c_x[n], c_y[n])$, generated by $c[n] = \sum_{m=0}^{n} w[m]$, where $w[n]$ is white Gaussian noise. Right: white uniform noise $(w_x[n], w_y[n])$. For all signals, $N = 50$.

Table 1. Nonstationary coupling parameters $c[n]$ and $d[n]$ for the 4 length-N simulated signals

	Signals			
Parameter	1	2	3	4
$c[n]$	0	$0.2H(n - N/2)$	$s[n]H\,(s[n])$	0
$d[n]$	$2a[n]s[n]$	$0.8[1 - H(n - N/2)]$	$\lvert\hat{s}[n]\rvert H\,(-\hat{s}[n])$	$a[n]$

Unit step function $H(n) = 1$ for $n \geq 0$ and $H(n) = 0$ for $H(n)$ for $n < 0$;
Sinusoidal signals $s[n] = 0.5\sin(2\pi n5/N)$ and $\hat{s}[n] = 0.5\sin(2\pi n5/N + \pi/2)$;
Damped exponential $a[n] = \mathrm{e}^{-n/(N/1.5)}$.

2.6. Numerical Examples

To validate our methods we provide numerical examples with different coupling scenarios. We use the following 2nd-order MVAR model

$$x[n] = 0.6x[n-1] - 0.91x[n-2] + c[n]y[n-1] + w_1[n] \tag{14a}$$

$$y[n] = 1.58x[n-1] - 0.96x[n-2] + d[n]x[n-1] + w_2[n] \tag{14b}$$

for $n = 0, 1, \ldots, N-1$ with zero-mean white Gaussian noise as the innovation process $\mathbf{w}[n]$. Parameters $c[n]$ and $d[n]$ set the time-varying coupling between $x[n]$ and $y[n]$. We generate 4 different examples, with $c[n]$ and $d[n]$ functions defined in Table 1. Examples 1–3 use the MVAR model in (14*a*, 14*b*); example 4 uses a time-varying definition of $x[n]$,

$$x[n] = 2\cos(2\pi f[n])x[n-1] - 0.91x[n-2] + w_1[n] \tag{15}$$

with time-varying frequency $f[n] = 0.15 + 0.2\sin(2\pi n0.5/N)$ and $y[n]$ defined in (14*b*). To validate the IF estimate approach in (8), we generate multiple (1 000) realisations of example signal 4 and use (8) to calculate the IF of the coupling.

2.7. Association with outcome

We relate all features of coupling, $\{d_1, d_2, \ldots, d_8\}$ generated from the detrend component and t_1 in (1) from trend component, to three clinical variables of interest: short-term

Accepted Manuscript

clinical outcome, GA of the infant, and inotrope use. Inotrope support is classified as a binary variable: yes or no if inotropes are administered within the first 24 hours.

As GA is a continuous variable we correlate age with all features $\{t_1, d_1, \ldots, d_8\}$. We use Spearman's correlation, defined in (1), with 95% confidence intervals (CIs) generated with 1 000 iterations of a bootstrap process. For consistency, we also use Spearman's correlation as an effect-size measure for outcome and inotrope-support variables. As outcome is of primary interest, we consider GA and inotropes as potential confounders. Van Laere *et al.* (2016) showed that both variables significantly ($P < 0.05$) differ for outcome groups. Therefore, if we find either variable is significantly associated with a particular feature, and this feature is also significantly associated with outcome, then we control for this potential confounder using multiple linear regression.

Independent features with sufficient potential are combined to detect outcome. We use a support vector machine with a linear kernel, training and testing over a leave-one-baby out cross-validation procedure. Regularisation parameter C is selected over the range of values $10^{-3}, 10^{-2}, \ldots, 10^{3}$ using a nested 5-fold cross-validation procedure. This parameter is scaled for 2 classes (normal and adverse outcome) in proportion to number of infants in each class. Features are converted to z-scores before training and testing, with testing using the mean and standard deviations estimated during training. Again, we consider GA and inotropes as potential confounders with the support vector model. Area under the receiver operator characteristic and Matthews correlation coefficient are used to evaluate performance of trained model.

All methods, including the numerical examples in Section 2.6, are available as Matlab computer code: https://github.com/otoolej/nonstat_directional_coupling.

3. Results

3.1. Proof-of-concept examples

Figure 2 presents the time–frequency ST-iPDC plots for 1 realisation of the 4 coupling examples for $x[n]$ and $y[n]$ in (14a, 14b) and (15). Also included in this figure is the spectral distributions for $x[n]$ and $y[n]$ and time-varying coupling parameters $c[n]$ and $d[n]$ detailed in Table 1. We can see in Figure 2 that when $c[n] = 0$ then $|S_{yx}[n,k]|^2 \approx 0$ for all k, for all 4 examples; and likewise, when $d[n] = 0$ then $|S_{xy}[n,k]|^2 \approx 0$ for all k. Thus the ST-iPDC is able track the nonstationary coupling. Example signals 1–3 in [Figure 2(a)–2(c)] show the time-varying coupling produced by the amplitude modulation parameters $c[n]$ and $d[n]$ but at a constant frequency. Example 4, in Figure 2(d), shows both amplitude- and frequency-modulation coupling as the ST-iPDC for $x \rightarrow y$ highlights the frequency-varying coupling produced by (15).

Figure 3(a) illustrates the IF estimates extracted from the ST-iPDC ($x \rightarrow y$) with frequency-varying coupling in Figure 2(d). This figure highlights the relative accuracy of the IF estimates, which uses the median frequency approach in (8), for this signal type.

Accepted Manuscript

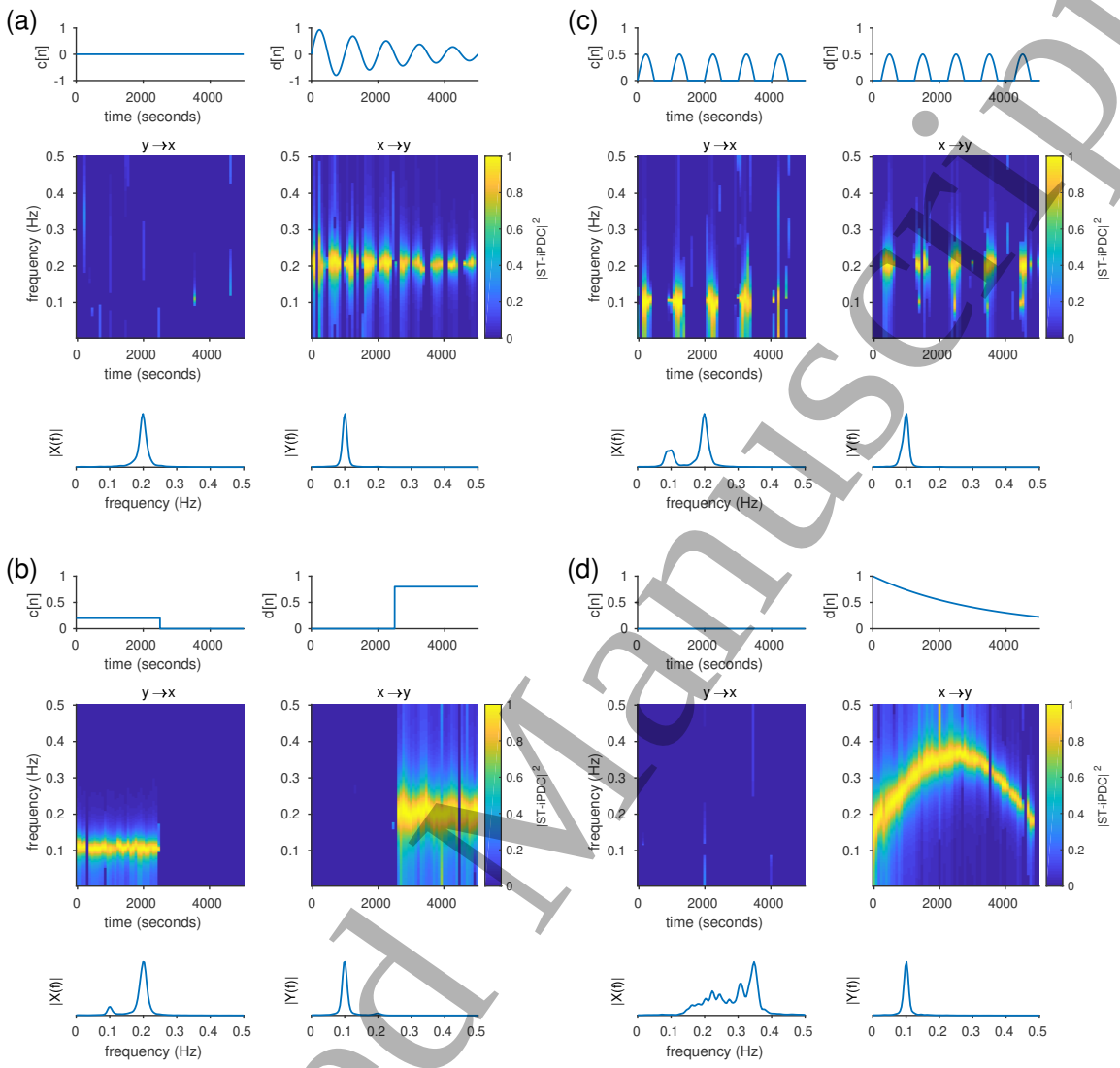


Figure 2. Nonstationary coupling for the short-time information partial directered coherence (ST-iPDC) for 4 test signals (a, b, c, and d for signals 1, 2, 3, and 4, respectively). Each sub-plot contains the coupling parameters $c[n]$ and $d[n]$ (top) from Table 1, the ST-iPDC (middle) for signals $x[n]$ and $y[n]$, and the auto-spectra for both signals (bottom).

Figures 3(b) and 3(c) shows the trajectory of the time-marginal of the ST-iPDC plotted as plane curves for signals 2 and 3 [Figures 2(b) and 2(c)]. These 2 curves capture the differences in time-varying coupling between the 2 signals: for signal 3, the predominant coupling is from $x \to y$ for the first half of the signal and then from $y \to x$ for the second half, in keeping with the coupling function $c[n]$ and $d[n]$ for this example (see Table 1); in contrast, the direction of the coupling for signal 3 cycles between $x \to y$ and $y \to x$, again in keeping with the defined coupling parameters.

Accepted Manuscript

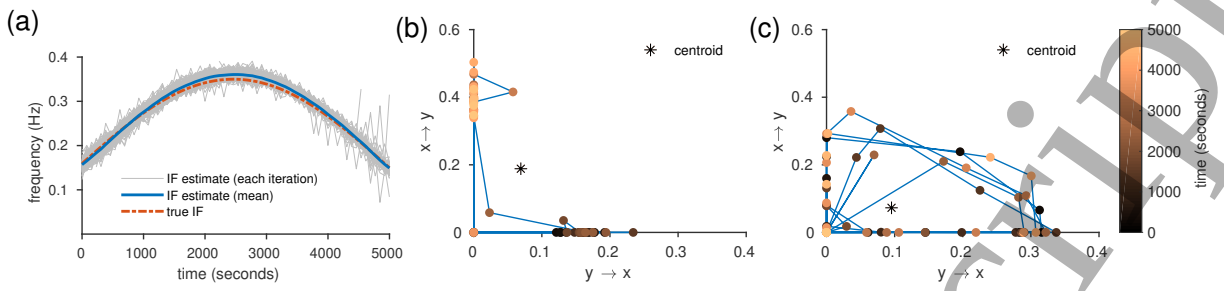


Figure 3. Time-varying coupling between test signals. (a): estimates of instantaneous frequency (IF) coupling for $x \to y$ in example 4 in Figure 2(d). Temporal evolution of the directional coupling in (b) and (c) for examples Figure 2(b) and Figure 2(c).

3.2. Physiological signals

From the cohort of 99 infants, 14 (14.1%) were classified into the adverse outcome group: 6 infants with severe IVH, 3 infants with periventricular leukomalacia, and 5 infants died within the first 3 days (Van Laere *et al.*, 2016). Fifteen (15.2%) of the infants were administered inotropes within the first 24 hours Van Laere *et al.* (2016). Inotrope administration is not associated with GA ($P = 0.122$, Mann–Whitney U-test). Further details on this cohort is available in Van Laere *et al.* (2016).

After artefact removal, the median percentage of missing data for the PI signal is 0.0% (IQR: 0.0 to 0.2%; range 0.0 to 0.9%) and 0.1% (IQR: 0.0 to 0.3%; range 0.0 to 7.7%) for the HR signal. (For the analysis we classified artefact as missing data.) Duration of HR–PI recordings is not associated with GA ($r = -0.04$, 95% CI: -0.24 to 0.15; $P = 0.724$). Figure 4 shows the associations between the HR and PI signals and the 3 clinical variables. HR decreases with GA ($r = -0.27$, 95% CI: -0.45 to -0.08; $P = 0.007$) and PI is significantly lower for those infants with adverse outcome comparative to those infants with normal outcome ($P = 0.002$).

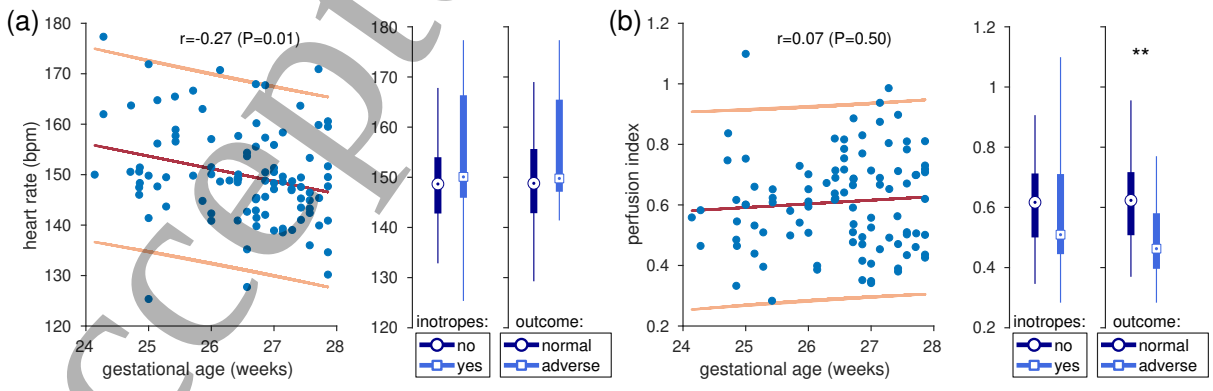


Figure 4. Distribution of the physiological signals in relation to gestational age, inotrope administration, and clinical outcome. Perfusion index in (a) and heart rate in (b) averaged over the 24 hour period. Statistical significance: ** for $P < 0.01$ from Mann–Whitney U-tests.

Accepted Manuscript

3.2.1. Analysis of trends Coupling for the HR and PI trend components, plotted in Figure 5(a), is non-zero ($P < 0.05$) for most infants (89/99), with a median value of $t_1 = 0.12$ (95% CIs: -0.69 to 0.82); where t_1 is Spearman's correlation defined in (1). Figure 5(b) shows the significant association between the 3 clinical variables and the coupling measure t_1. Adverse clinical outcome is associated with a decrease in coupling of the trend components: correlation $r = -0.23$ with 95% CI of -0.41 to -0.03 ($P = 0.026$). Increasing GA is associated with increasing coupling ($r = 0.23$, 95% CI: 0.03 to 0.42; $P = 0.022$). And lastly, inotrope administration is associated with a decrease in coupling ($r = -0.35$, 95% CI: -0.51 to -0.15; $P < 0.001$).

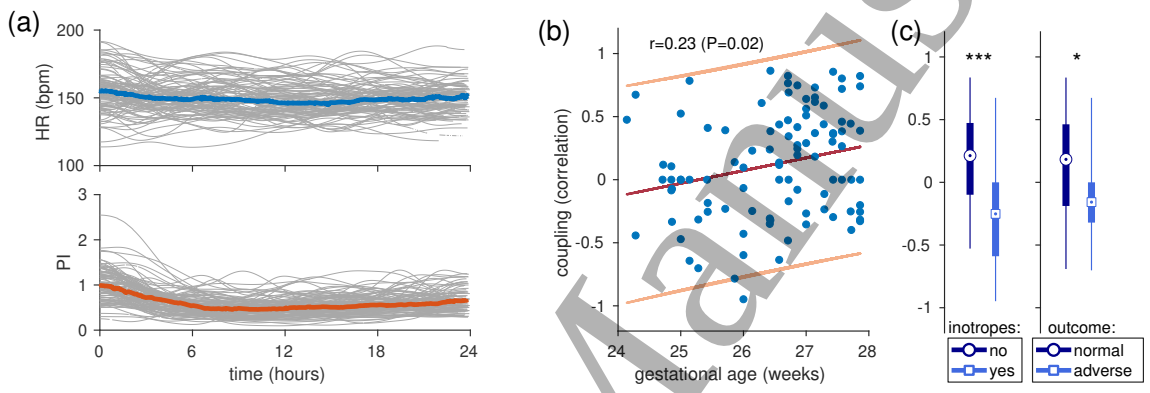


Figure 5. Trend components for heart rate (HR) and perfusion index (PI) in (a) for all infants ($n = 99$). Thick lines represent the median value. Coupling between HR and PI trends and its relation to gestational age in (b), and inotrope use and clinical outcome in (c). Coupling is measured by Spearman's correlation. Statistical significance in (c): $*$ for $P < 0.05$ and $***$ for $P < 0.001$ from Mann–Whitney U-tests.

As both GA and inotropes are significantly correlated with t_1, and therefore potential confounders, we fit a multiple linear regression model including GA, inotrope use, and outcome as independent variables with the coupling measure t_1 as the dependent variable. We transform t_1 and GA as they negatively skewed using the following expression

$$y = \log_{10}\{\max(x) + 1 - x\} \tag{16}$$

which transforms x to an approximately Gaussian distributed variable y. Estimates of the coefficients in Table 2 show that when controlling for GA and inotrope use, outcome is no longer a significant variable in relation to t_1, the coupling measure between HR and PI trends.

3.2.2. Nonstationary and directional coupling The MVAR model in (2) fits the HR and PI detrend components in most cases: a median of 8.6% (95th centile range: 0% to 22.1%) epochs per recording were excluded from analysis because the residuals, $\mathbf{w}[n]$ in (2), were significantly correlated ($P < 0.05$). Analysis of the ST-iPDC showed weak but significant coupling in both directions, as illustrated in Figure 6. The coupling from HR $\rightarrow$ PI, with median coherence values of 0.022 (IQR: 0.012 to 0.030), is greater than

Accepted Manuscript

Table 2. Linear regression coefficients with t_1 (correlation between HR and PI trend component) as the dependent variable.

	estimate (95% CI)	P-value
intercept	0.18 (0.14 to 0.22)	<0.001
outcome‡	0.019 (-0.047 to 0.084)	0.576
inotropes§	0.092 (0.029 to 0.16)	0.005
GA†	0.097 (-0.015 to 0.208)	0.090

† Gestational age (GA) transformed using equation (16) to better approximate a Gaussian distribution (as is dependent variable t_1).
‡ Reference value is normal outcome.
§ Reference value is absence of inotropes.

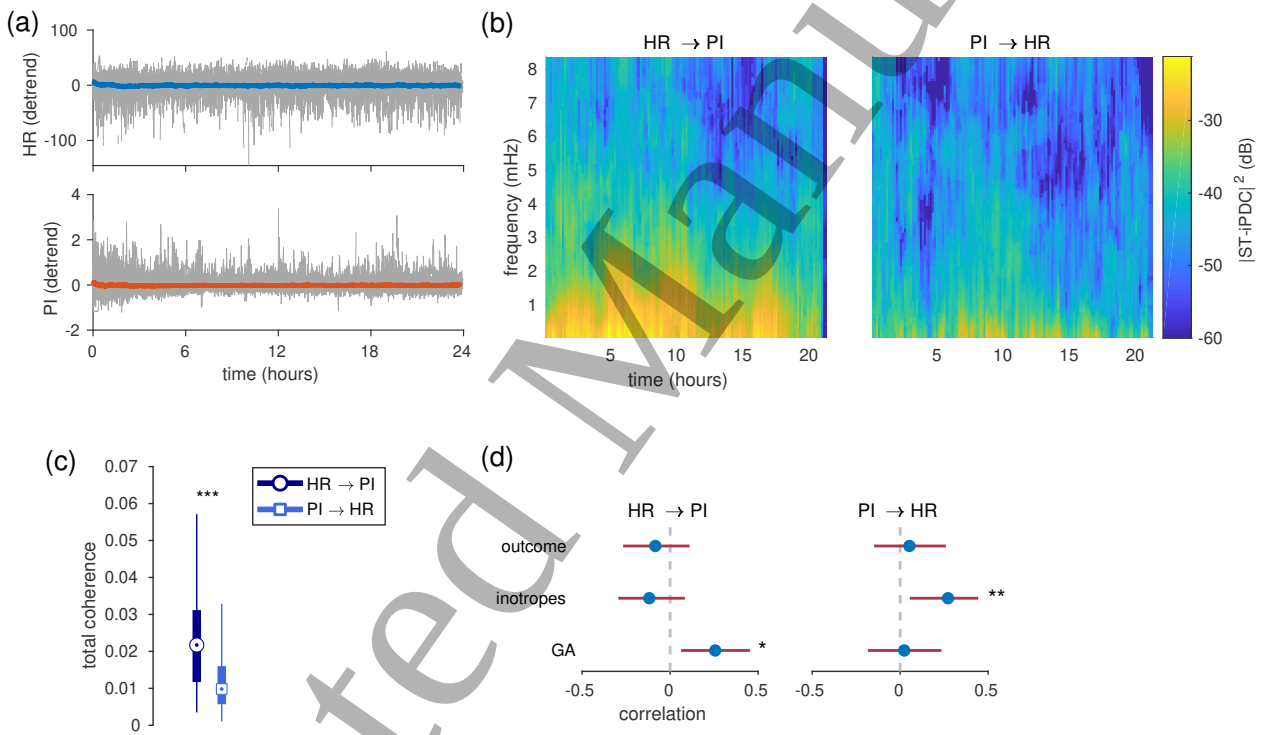


Figure 6. Total coherence for the detrend components of heart rate (HR) and perfusion index (PI) signals. A: detrend components for all infants ($n = 99$); thick lines represent the median value. B: short-time information partial directed coherence (ST-iPDC) averaged over all infants. C: total coherence, estimating by summing ST-iPDC over the time–frequency plane, is larger for direction HR → PI compared to PI → HR; dots: median values, thick lines: inter-quartile range, thin lines: 95th centile range. D: influence of gestational age (GA), clinical outcome, and inotrope use on total coherence; Spearman's correlation (x-axis) is used as an effect size. Binary variables outcome and inotropes are coded as 1 for adverse clinical outcome and inotrope administration. Statistical significance: $*$ for $P < 0.05$, $**$ for $P < 0.01$, and $***$ for $P < 0.001$ from Mann–Whitney U-tests.

the PI → HR coupling values, with median coherence values of 0.010 (IQR: 0.006 to 0.015), with $P < 0.001$; see boxplot in Figure 6.

Accepted Manuscript

If we compare the total coherence, estimated by summing ST-iPDC across time and frequency, for the 3 clinical variables of interest, we find that total coherence for HR $\rightarrow$ PI significantly increases with GA ($r = 0.26$, with 95% CIs of 0.05 to 0.42; $P = 0.011$) and that total coherence for PI $\rightarrow$ HR is significantly greater for those infants administered inotropes ($r = 0.27$, with 95% CIs of 0.06 to 0.46; $P = 0.007$). All correlation values for total coherence are plotted in Figure 6(d).

The results for IF features, $\{d_1, d_2, d_3, d_4\}$ from (9)–(11), are presented in Figure7(a). None of the IF features are significant for the HR $\rightarrow$ PI coupling. But for the PI $\rightarrow$ HR coupling, 3/4 IF features are significant for clinical outcome. For infants with adverse outcome, there is an increase in the standard deviation of the IF ($r = 0.26$, 95% CI: 0.09 to 0.41; $P = 0.012$) and mobility of the IF ($r = 0.27$, 95% CI: 0.08 to 0.43; $P = 0.009$), and a decrease in IF complexity ($r = -0.20$, 95% CI: -0.35 to -0.03; $P = 0.049$). The features $\{d_6, d_7, d_8\}$ that represent the temporal trajectory of coherence between HR $\rightarrow$ PI and PI$\rightarrow$HR are presented in Figure 7(b). Inotrope administration is associated with an increase in fractal dimension ($r = 0.27$, 95% CI: 0.01 to 0.44; $P = 0.008$) and angle of the centroid ($r = 0.28$, 95% CI: 0.07 to 0.47; $P = 0.005$) feature. GA is negatively associated with fractal dimension: decreasing fractal dimension with increasing GA ($r = -0.20$, 95% CI: -0.41 to 0.01; $P = 0.049$).

In comparison to the Granger causality measures, we find no significant association between the 3 clinical variables and metrics of the short-time coherence function $C_{lq}[n, k]$ from (6)–(7). Details are provided in Section Appendix A (Supplementary Material).

3.2.3. Detection of outcome The 4 features of nonstationary coupling $\{d_1, d_2, d_3, d_4\}$ for PI$\rightarrow$HR from Figure 7(a) are combined in the linear support vector machine to detect short-term clinical outcome. Mean PI, from Figure 4(b), is also included in this model. Table 3 presents detection performance for the individual features and the cross-validation testing results for the trained model. The most common value for regularisation parameter C was 0.1, selected 74/99 times in the nested 5-fold iterations. The trained model was not significantly associated with GA ($r = -0.08$, 95% CI: -0.26 to 0.13; $P = 0.476$) or inotrope support ($r = 0.17$, 95% CI:-0.02 to 0.35; $P = 0.078$). Because inotrope support is close to significance, with $P < 0.1$, we test as a potential confounder. We include inotrope support and clinical outcome as independent variables in a linear regression model with output of the trained support vector machine as the dependent variable. Clinical outcome retains significant: regression coefficient for outcome is 1.06 (95% CI of 0.49 to 1.63; $P < 0.001$).

4. Discussion

This is the first study to explore coupling between HR and PI in extremely preterm infants over the first 24 hours of life. We find weak but significant coupling in both the HR$\rightarrow$PI and PI$\rightarrow$HR directions [Figure 2(b)]. Although HR$\rightarrow$PI coupling is significantly stronger than PI$\rightarrow$HR coupling [Figure 2(c)], nonstationary features of

Accepted Manuscript

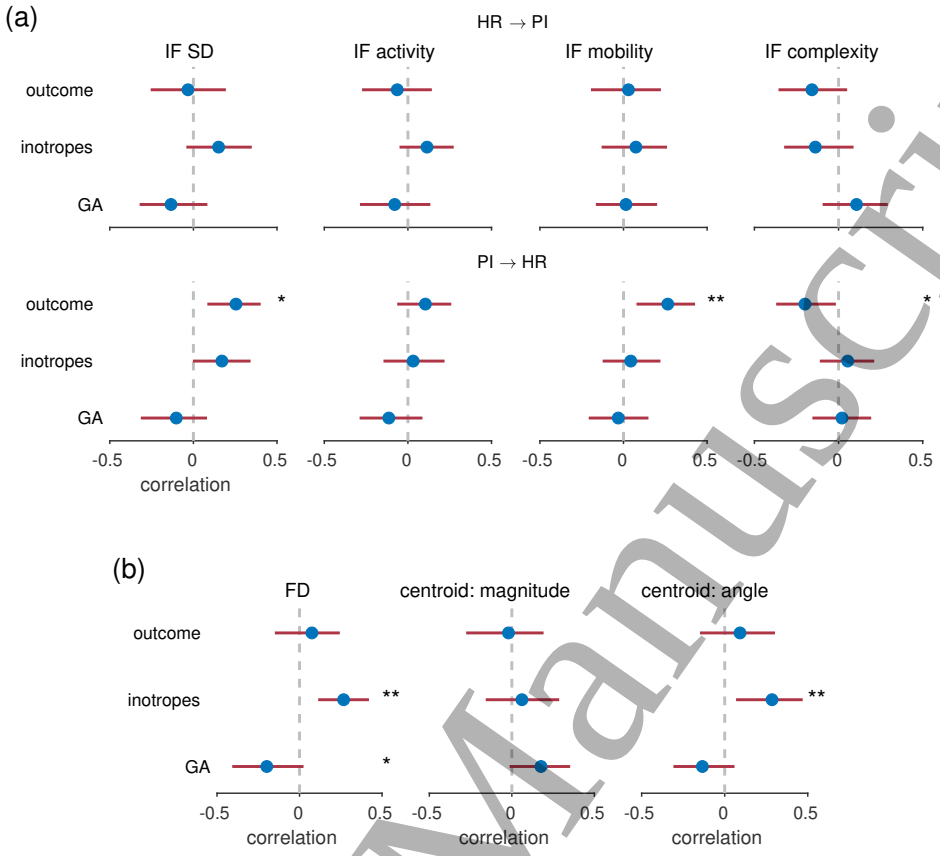


Figure 7. Non-stationary measures of coupling and association with clinical outcome, inotrope use, and gestational age (GA). A: 4 features of coupling are estimated from the time-varying coherence function: standard deviation of the instantaneous frequency (IF) from the short-time iPDC and the 3 Hjorth parameters of the IF, namely activity, mobility, and complexity. Top row for features of the coupling with heart rate (HR) influencing perfusion index (PI), and bottom row for PI influencing HR. B: 3 features that summarise the trajectory of the time-marginal time-varying coherence function, namely fractal dimension (FD), the magnitude of the centroid, and the angle of the centroid. Binary variables outcome and inotropes are coded as 1 for adverse clinical outcome and inotrope administration. Dots represent Spearman's correlation coefficient with 95% confidence intervals (bars), used here as an effect size measure. Significance: $*$ for $P < 0.05$, $**$ for $P < 0.01$, and $***$ for $P < 0.001$ from Mann–Whitney U-tests.

PI→HR coupling show an association with clinical outcome that is independent of GA and inotrope administration. Causality is an important component of our analysis as we untangle the interaction between these 2 physiological signals. For example, we find that HR→PI coupling increases with maturation and PI→HR coupling increases with inotrope administration [Figure 6(d)]. Coherence, without a measure of causality, shows no association with any of the 3 clinical variables (Figure A1). We also find that the ultra-slow oscillations of HR and PI, signals with periods >12 hours, are correlated [Figure 5(b)] and that this association changes with inotropic therapy. Those infants receiving inotropes will tend to have a negative HR–PI correlation compared

Accepted Manuscript

Table 3. Detection performance of individual features and cross-validation testing results for the combination of all features using a support vector machine (SVM).

Feature/method	MCC	AUC	Sensitivity (%)	Specificity (%)	PPV (%)	NPV (%)
Mean PI	0.339	0.766	74.1	71.4	94.0	31.2
IF SD†	0.317	0.710	71.4	71.8	29.4	93.8
IF activity†	0.021	0.586	50.0	52.9	14.9	86.5
IF mobility†	0.339	0.720	71.4	74.1	31.2	94.0
IF complexity†	0.121	0.663	60.0	57.1	89.5	19.0
SVM	0.518	0.866	85.7	81.2	42.9	97.2

†Nonstationary features of instantaneous frequency (IF) estimated from PI→HR coupling.
Key: MCC, Matthews correlation coefficient; AUC, area under the receiver operator characteristic; PPV, positive predictive value; NPV, negative predicative value; IF, instantaneous frequency; SD, standard deviation.

to those not receiving the therapy who tend to have a positive HR–PI correlation [Figure 5(b)]. Combining features of nonstationary coupling with mean PI in a machine learning algorithm provides detection of adverse outcome with a sensitivity of 85.7% and specificity of 81.2%.

Accounting for the nonstationarity of these long-duration (24 hours) physiological signals is a key component in our approach. We extended the iPDC to include time-varying coherence by applying a short-time windowing approach. This approach assumes that the signals are stationary within the window duration, an untested assumption for our data. There are alternatives to the short-time appoach, for example by developing a time-varying MVAR model for partial-directed coherence functions (Pagnotta and Plomp, 2018). We use this short-time approach for 2 reasons. First, the time-varying parameters are more difficult to fit than stationary MVAR models, and in practice we have found this to be a challenge in other applications (Omidvarnia *et al.*, 2011, 2014). And second, the time-varying MVAR models do not always produce more accurate time–frequency coherence distributions (Omidvarnia *et al.*, 2011). In other areas of signal processing, the short-time approach is the most common approach for the analysis of nonstationary signals: for example the spectrogram is a tried-and-trusted time–frequency analysis tool very much still in use today. In addition, the numerical examples in Figure 2 validate our approach, as the expected time–frequency patterns are evident for all test signals.

Another important aspect of our analysis is the feature set. Although many coupling methods are nonstationary they fail to extract features of the time–frequency coupling (Pagnotta and Plomp, 2018; Beausoleil *et al.*, 2018; Placek *et al.*, 2017; Formaggio *et al.*, 2014; Schiecke *et al.*, 2016; Omidvarnia *et al.*, 2014; Chang and Glover, 2010). For example, nonstationary coupling is often used as a visual identification tool to locate regions of interest in the time–frequency plane and then average over this region (Piper

Accepted Manuscript

et al., 2014; Formaggio *et al.*, 2014; Omidvarnia *et al.*, 2014). Summing across time and frequency will generate a metric of coupling that ignores the time and frequency trajectories, and is unable to distinguish between 2 very different modes of coupling: for example, between the 2 test signals in Figures 2(b) and 2(c). We propose a feature set that quantifies the nonstationary characteristics of coupling and is therefore able to distinguish between fundamentally different modes of time–frequency coupling. The 4 IF features [Figure 7(a)] characterise the temporal trajectory of the frequency-dependent coupling. The 3 features of the time-marginals [Figure 7(b)] characterises the temporal trajectory of the direction-dependent coupling. With this proposed feature set we can uncover and quantify the time-varying relation between the signals. For example, it is clear from the numerical examples in Figure 2 that only nonstationary features can distinguish between the time-varying coupling in the different examples, as shown in Figure 3.

In addition to developing methods to quantify nonstationary and directional coupling between HR and PI, we also trained a machine-learning model to detect clinical outcome. The model uses features of nonstationary PI→HR coupling and mean PI over the 24 hours; we include mean PI as it was significantly associated with outcome but not with inotrope support or GA. Detection performance, assessed by Matthews correlation coefficient, for the individual features ranged from 0.02 to 0.34 (Table 3). Combining these features in the support vector machine increased the correlation coefficient to 0.52. We developed the model to highlight the potential of coupling features as biomarkers of adverse outcome. Future work could include a more extensive feature set including other characteristics of HR and PI, trained and tested on a large data set.

It is not surprising to find that the predominant causality is from HR→PI, and not PI→HR. As the cell structure of the myocardium of a preterm infant is in an embryological state of development (Anderson, 1996) it affects the ability to increase its stroke volume in the presence of changing loading conditions at birth (Poon *et al.*, 2019; Eriksen *et al.*, 2014). As such, organ blood flow (reflected in PI) is substantially influenced by changes in HR and vascular tone (Winberg and Ergander, 1992; De Waal *et al.*, 2017). The cardiovascular tone is controlled by the autonomous nervous system (Mulkey and dú Plessis, 2018) that allows for the redistribution of blood flow to vital organs by affecting cardiac output or peripheral vascular tone. This complex process is mediated by activating adrenergic/cholinergic receptors (A/C-R) present on the heart and the peripheral vessels. In prematurity it is unclear whether these receptors are functionally matured (Patural *et al.*, 2008) which could explain our finding that the HR→PI relation strengthens with gestational age [Figure 6(d)]. Prematurity could also be reflected in a maturational A/C-R imbalance (Hunt, 2006) which could explain the more surprising significant coupling between PI→HR [Figures 6(b) and 6(c)]. The effect of inotropic medication on the circulation is exerted in a dose-dependent activation of the A/C-R. The effect of blood pressure augmentation therapy, mainly known from adult physiology, could therefore be different in preterm infants than anticipated (Eiby *et al.*, 2016) and reflected in the finding that PI→HR coupling increases with inotrope

Accepted Manuscript

administration [Figure 6(d)]. But we lack certainty as we are speculating about a complex biomedical system based on data recorded from limited peripheral locations from immature newborns during extra-uterine adaptation.

Similarly it is also difficult to relate the nonstationary features of time-varying coupling to a physiological process. The feature set was designed to capture the nonstationary and directional characteristics of the coupling. We find that features of the IF for PI→HR coupling are associated with outcome. The complex nature of these features may preclude a direct link to the underlying physiology, other than stating that the differences in the temporal pathway in cardiovascular physiology likely indicate haemodynamic instability and hence the association with adverse outcome. None of the 3 direction-dependent features were associated with outcome, but we do find that inotrope administration increases the level of disorder, as measured by fractal dimension, between the direction-dependent causality of HR→PI and PI→HR [Figure 7(b)]. In contrast, this level of disorder decreases with maturation [again Figure 7(b)].

The ST-iPDC function evaluates time-varying Granger causality. This stationary iPDC function estimates a normalised effect-size measure of coherence that is amplitude-invariant, unlike other directed coherence functions (Takahashi *et al.*, 2010). We also implement the closed-form statistical approach to remove non-significant coherence values from the ST-iPDC (Baccala *et al.*, 2013). There are, however, many other methods to test for causality (Hassan and Wendling, 2018; Greenblatt *et al.*, 2012). For example, wavelet coherence functions generate time–scale representations of coherence (Beausoleil *et al.*, 2018; Piper *et al.*, 2014). Wavelets provide poor representations of the time–frequency plane (Boashash and Ouelha, 2018) and singularities, from the normalisation process, make interpretation difficult (Beausoleil *et al.*, 2018; Chang and Glover, 2010). Our ST-iPDC function, in contrast, does not produce singularities and has good time–frequency resolution, as shown in Figure 2. Coherence methods specific to signal types are also available. For example, Omidvarnia *et al.* (2014) developed non-stationary coherence methods to specifically avoid the volume conduction problem in EEG. Volume conduction is not applicable to our signals however. The most significant limitation of our approach here is that we assess for linear coupling only, and do not test for nonlinear coupling. We leave this analysis for future work.Another limitation is that we examine this coupling only on day 1, in keeping with our previous study on PI (Van Laere *et al.*, 2016). As pathologies such as IVH are likely to develop over the first few days of life, future studies should include this extended time frame to map temporal evolutionary pathways of the HR–PI coupling and its association with adverse outcome.

5. Conclusions

This is the first study to examine the interaction between HR and PI in a large cohort ($n = 99$) of extremely preterm infants. We develop features which quantify time-varying and direction-varying interactions, necessary for characterising coupling in complex biological systems. Our results present new findings on the interaction

Accepted Manuscript

between these physiological signals during postnatal adaptation and identify potential biomarkers of adverse outcome, including brain injury. This is significant as these features are objective markers extracted from existing monitoring technologies common to many neonatal intensive care units. Early detection of injury during the postnatal transition could improve critical care and therefore long-term clinical outcome for this group of vulnerable infants.

Acknowledgments

JMOT was supported by Science Foundation Ireland (15/SIRG/3580).

References

Alderliesten T, Lemmers P M A, Baerts W, Groenendaal F and van Bel F 2015 Perfusion Index in Preterm Infants during the First 3 Days of Life: Reference Values and Relation with Clinical Variables *Neonatology* **107**(4) 258–65

Anderson P A 1996 The heart and development, *Semin. Perinatol.* **20**(6) 482–509

Baccala L A, de Brito C S N, Takahashi D Y and Sameshima K 2013 Unified asymptotic theory for all partial directed coherence forms *Philos. Trans. Royal Soc. A* 371:20120158

Beausoleil T P, Janaillac M, Barrington K J, Lapointe A and Dehaes M 2018 Cerebral oxygen saturation and peripheral perfusion in the extremely premature infant with intraventricular and/or pulmonary haemorrhage early in life *Sci. Rep.* **8**(1) 6511

Boashash B and Ouelha S 2018 Designing high-resolution time–frequency and time–scale distributions for the analysis and classification of non-stationary signals: a tutorial review with a comparison of features performance *Digital Signal Process.* **77** 120–52

Bolisetty S, Dhawan A, Abdel-Latif M, Bajuk B, Stack J and Lui K 2014 Intraventricular hemorrhage and neurodevelopmental outcomes in extreme preterm infants *Pediatrics* **133**(1) 55–62

Chang C and Glover G H 2010 Time-frequency dynamics of resting-state brain connectivity measured with fMRI *NeuroImage* **50**(1) 81–98

Cresi F, Pelle E, Calabrese R, Costa L, Farinasso D and Silvestro L 2010 Perfusion index variations in clinically and hemodynamically stable preterm newborns in the first week of life *Ital. J. Pediatr.* **36** 6

De Waal K, Phad N, Lakkundi A and Tan P 2017 Post-transitional adaptation of the left heart in uncomplicated, very preterm infants *Cardiol. Young* **27**(6) 1167–73

Eiby Y A, Shrimpton N Y, Wright I M, Lumbers E R, Colditz P B, Duncombe G J and Lingwood B E 2016 Inotropes do not increase cardiac output or cerebral blood flow in preterm piglets *Pediatr. Res.* **80**(6) 870–79

Accepted Manuscript

Eriksen B H, Nestaas E, Hole T, Liestøl K, Støylen A and Fugelseth D 2014 Myocardial function in term and preterm infants. Influence of heart size, gestational age and postnatal maturation *Early Hum. Dev.* **90**(7) 359–64

Formaggio E, Storti S F, Boscolo Galazzo I, Gandolfi M, Geroin C, Smania N, Fiaschi A and Manganotti P 2014 Time–Frequency Modulation of ERD and EEG Coherence in Robot-Assisted Hand Performance *Brain Topogr.* **28**(2) 352–363

Gill A W 2019 Postnatal cardiovascular adaptation *Arch. Dis. Child. Fetal Neonatal Ed.* **104**(2) F220–24

Greenblatt R E, Pflieger M E and Ossadtchi A E 2012 Connectivity measures applied to human brain electrophysiological data *J. Neurosci. Methods* **207**(1) 1–16

Hassan M and Wendling F 2018 Electroencephalography Source Connectivity: Aiming for High Resolution of Brain Networks in Time and Space *IEEE Signal Process. Mag.* **35**(3) 81–96

Hawkes G A, O'Toole J M, Kenosi M, Ryan C A and Dempsey E M 2015 Perfusion index in the preterm infant immediately after birth *Early Hum. Dev.* **91**(8) 463–65

Hendrikx D, Thewissen L, Smits A, Naulaers G, Allegaert K, Van Huffel S and Caicedo A 2018 Using Graph Theory to Assess the Interaction between Cerebral Function, Brain Hemodynamics, and Systemic Variables in Premature Infants *Complexity* **2018** 6504039

Higuchi T 1990 Relationship between the fractal dimension and the power law index for a time series: a numerical investigation *Physica D* **46** 254–64

Hjorth B 1970 EEG analysis based on time domain properties *Electroencephalogr. Clin. Neurophysiol.* **29**(3) 306–10

Hunt C E 2006 Ontogeny of autonomic regulation in late preterm infants born at 34–37 weeks postmenstrual age *Semin. Perinatol.* **30**(2) 73–6

Iyer K K, Roberts J A, Hellström-Westas L, Wikström S, Hansen Pupp I, Ley D, Breakspear M and Vanhatalo S 2015 Early Detection of Preterm Intraventricular Hemorrhage From Clinical Electroencephalography *Crit. Care Med.* **43**(10) 2219–27

Katheria A C, Harbert M J, Nagaraj S B, Arnell K, Poeltler D M, Brown M K, Rich W, Hassen K O and Finer N 2018 The Neu-Prem Trial: Neuromonitoring of Brains of Infants Born Preterm During Resuscitation—A Prospective Observational Cohort Study *J. Pediatr.* **198** 209–213.e3

Kenosi M, O'Toole J M, Hawkes G A, Hutch W, Low E, Wall M, Boylan G B, Ryan C A and Dempsey E M 2017 Monitoring cerebral oxygenation of preterm infants using a neonatal specific sensor *J. Perinatol.* **38** 264–70

Kinoshita M, Hawkes C P, Ryan C A and Dempsey E M 2013 Perfusion index in the very preterm infant *Acta Paediatr.* **102**(9) e398–e401

Mulkey S B and dú Plessis A 2018 The critical role of the central autonomic nervous system in fetal-neonatal transition *Semin. Pediatr. Neurol.* **28** 29–37

Accepted Manuscript

Neumaier A and Schneider T 2001 Estimation of parameters and eigenmodes of multivariate autoregressive models. *ACM Trans. Math. Softw.* **27**(1) 27–57

Omidvarnia A, Azemi G, Boashash B, O' Toole J, Colditz P and Vanhatalo S 2014 Measuring time-varying information flow for scalp EEG signals: orthogonalized partial directed coherence *IEEE Trans. Biomed. Eng.* **61**(3) 680–93

Omidvarnia A, Mesbah M, O'Toole J M, Colditz P, and Boashash B 2011 Analysis of the time-varying cortical neural connectivity in the newborn EEG: a time-frequency approach *Int. Work. Sys. Signal Process. Appl.* IEEE Tipaza 1–4

O'Toole J M and Boylan G B 2017 NEURAL: quantitative features for newborn EEG using Matlab arXiv:1704.05694 [physics.med-ph]

O'Toole J M, Dempsey E M and Boylan G B 2018 Extracting transients from cerebral oxygenation signals of preterm infants: a new singular-spectrum analysis method *Int. Conf. IEEE Eng. Med. Biol. Soc.* IEEE Berlin 5882–5

O'Toole J M, Kenosi M, Finn D, Boylan G B and Dempsey E M 2016 Features of cerebral oxygenation detects brain injury in premature infants *Int. Conf. IEEE Eng. Med. Biol. Soc.* IEEE Orlando 3614–7

Pagnotta M F and Plomp G 2018 Time-varying MVAR algorithms for directed connectivity analysis: Critical comparison in simulations and benchmark EEG data *PLoS ONE* **13**(6) e0198846

Patural H, Pichot V, Jaziri F, Teyssier G, Gaspoz J M, Roche F and Barthelemy J C 2008 Autonomic cardiac control of very preterm newborns: A prolonged dysfunction *Early Hum. Dev.* **84**(10) 681–7

Piper D, Schiecke K, Pester B, Benninger F, Feucht M and Witte H 2014 Time-variant coherence between heart rate variability and EEG activity in epileptic patients: An advanced coupling analysis between physiological networks *New J. Phys.* **16**(11) 115012

Placek M M, Wachel P, Iskander D R, Smielewski P, Uryga A, Mielczarek A, Szczepański T A and Kasprowicz M 2017 Applying time–frequency analysis to assess cerebral autoregulation during hypercapnia *PLoS ONE* **12**(7) e0181851

Poon C Y, Wilson D G, Joshi S, Fraser A G and Kotecha S 2019 Longitudinal evaluation of myocardial function in preterm infants with respiratory distress syndrome *Echocardiography* **36**(9) 1713–26

Schiecke K, Pester B, Piper D, Benninger F, Feucht M, Leistritz L and Witte H 2016 Nonlinear Directed Interactions between Heart Rate Variability and EEG Activity in Children with Temporal Lobe Epilepsy *IEEE Trans. Biomed. Eng.* **63**(12) 2497–504

Schneider T and Neumaier A 2001 Algorithm 808: ARfit—a matlab package for the estimation of parameters and eigenmodes of multivariate autoregressive models *ACM Trans. Math. Softw.* **27**(1) 58–65

Stoll B J *et al.* 2010 Neonatal Outcomes of Extremely Preterm Infants From the NICHD Neonatal Research Network *Pediatrics* **126**(3) 443–56

Accepted Manuscript

Takahashi D Y, Baccalá L A and Sameshima K 2010 Information theoretic interpretation of frequency domain connectivity measures *Biol. Cybern.* **103**(6) 463–9

Van Laere D, O' Toole J M, Voeten M, McKiernan J, Boylan G B and Dempsey E M 2016 Decreased Variability and Low Values of Perfusion Index on Day One Are Associated with Adverse Outcome in Extremely Preterm Infants *J. Pediatr.* **178** 119–24

Van Laere D, Voeten M, O'Toole J M and Dempsey E M 2018 Monitoring Circulation During Transition in extreme Low Gestational Age newborns: what's on the Horizon? *Front. Pediatr.* **6** 74

Winberg P and Ergander U 1992 Relationship between heart rate, left ventricular output, and stroke volume in preterm infants during fluctuations in heart rate *Pediatr. Res.* **31**(2) 117–20

Accepted Manuscript

Appendix A. Nonstationary features of non-directed coherence

Figure A1 shows the grand-average of $C_{lq}[n,k]$ over all babies [Figure 1(a)] and association between total coherence ($C_{lq}[n,k]$ summed over time and frequency) with the 3 clinical variables.

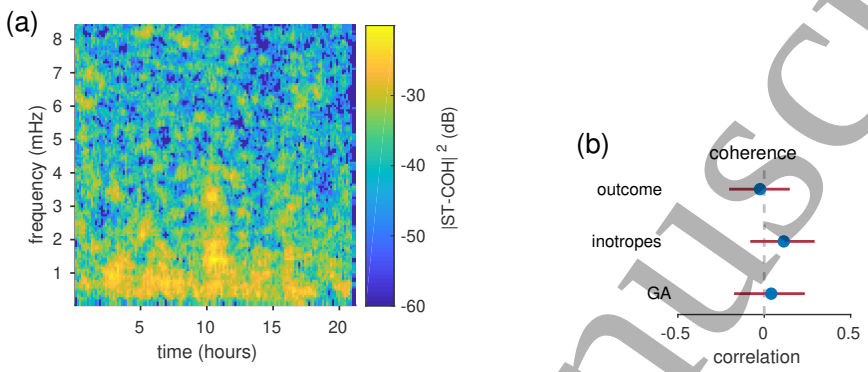


Figure A1. Coherence between the heart rate and perfusion index. (a): grand-average of the short-time coherence (ST-COH) function for all infants ($n = 99$). (b): influence of the clinical outcome, inotrope therapy, and gestational age (GA) on the coherence (total coherence summed over time and frequency); dots represent Spearman's correlation coefficient with 95% confidence intervals (bars), used here as an effect size measure. Binary variables outcome and inotropes are coded as 1 for adverse clinical outcome and inotrope administration. None of the variables in (b) are statistical significant (Mann–Whitney U tests, $P > 0.05$).

Figure A2 shows the relation between the IF features, $\{d_1, d_2, d_3, d_4\}$ in (9)–(10), and the 3 clinical variables. The IF is estimated from the short-time coherence function in (6)– (7). We found no statistical association among the features and the 3 clinical variables ($P > 0.05$).

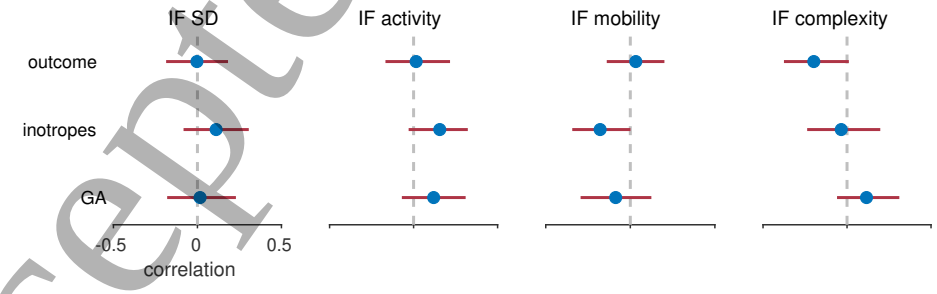


Figure A2. Non-stationary measures of coupling and association with clinical outcome, inotrope use, and gestational age (GA). The 4 features of coupling are estimated from the short-time coherence function: standard deviation of the instantaneous frequency (IF) from the coherence function and the 3 Hjorth parameters of the IF, namely activity, mobility, and complexity. Dots represent Spearman's correlation coefficient with 95% confidence intervals (bars), used here as an effect size measure. Binary variables outcome and inotropes are coded as 1 for adverse clinical outcome and inotrope administration. None of the variables are statistically significant (Mann–Whitney U tests, $P > 0.05$).

Accepted Manuscript